JMEPEG
https://doi.org/10.1007/s11665-022-06763-y

1059-9495/$19.00

TECHNICAL ARTICLE

Effect of Phosphorous Ion Implantation on the Surface, Crystal Structure, Mechanical, and Electrochemical Properties of Bioresorbable Magnesium for Biomedical Applications

Mazhar H. Asdi, M. Umar Aslam Khan, Javed Hussain, Muhammad Arshad, M. Ramzan Abdul Karim, Khalid Javed, Abdul Rehman, Ahsan Shafique, Shazia Bashir, and Saqlain A. Shah

Submitted: 31 August 2021 / Revised: 27 December 2021 / Accepted: 14 February 2022

Surface attributes of pure Mg such as biocompatibility, mechanical strength and corrosion are clinically important for artificial implants, but its fast degradation post-implantation has drawbacks. Tuning Mg for clinical needs is achieved by techniques like near surface ion implantation. This work is about improving the surface and corrosion rate of bioresorbable magnesium by phosphorous (*P*) ion implantation with fluences of 10^{16}-10^{18} ions/cm^2 and ion beam accelerating energy of $\sim$ 700 keV by a Pelletron Linear Accelerator. The in vitro degradation rate was examined using electrochemical potential tests in simulated body fluid (SBF). X-ray diffraction and energy-dispersive x-ray spectroscopy confirmed the implantation of *P* ions by forming an amorphous *P*-layer on the Mg surface. Surface hardness and electrochemical resistance improved as confirmed by the mechanical and electrochemical tests in SBF, respectively, post-implantation. Medical implants designed by this modified Mg are compliant with the patient's healing span post-implantation with decreased corrosion rate agreeing with the healing process, avoiding an implant removal surgery post-patient's recovery.

Mazhar H. Asdi, Khalid Javed, Abdul Rehman, and **Saqlain A. Shah**, Department of Physics, Forman Christian College (University), Lahore, Pakistan; **M. Umar Aslam Khan**, School of Biomedical Engineering and Health Sciences, Universiti Teknologi Malaysia, Johor Bahru, Johor, Malaysia; **Javed Hussain** and **Muhammad Arshad**, National Center for Physics, Islamabad, Pakistan; and **M. Ramzan Abdul Karim**, GIK Institute of Engineering Sciences and Technology, Topi, Pakistan; **Ahsan Shafique** and **Shazia Bashir**, Center for Advanced Studies in Physics, Government College University, Lahore, Pakistan. Contact e-mails: Muhammad.arshad@ncp.edu.pk saqlain007pk@hotmail.com.

Published online: 31 March 2022

Graphical Abstract

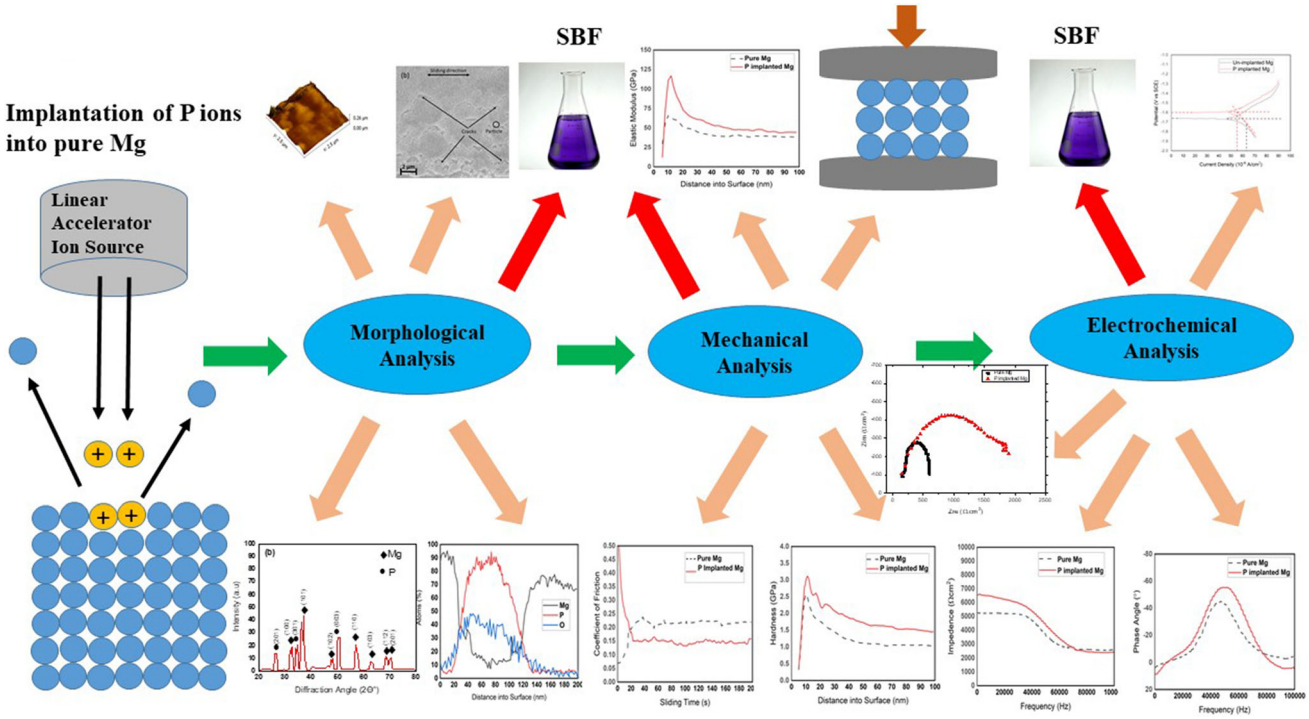

Keywords bioresorbable, electrochemical, ion implantation, mechanical properties, morphology

1. Introduction

Bioresorbable metals such as magnesium (Mg) are of paramount importance regarding their applicability as biomedical implants such as cardiovascular stents, and orthopedic or dental implants. The mechanical properties such as elastic modulus and density of magnesium comply with the human bone. As a result, the stress-shielding effect of magnesium-based implants is comparable with the human bone which is important for the natural healing of the bone tissues as the implant material dissolves with the bone. Also, unlike the traditional passive metals such as titanium, due to its natural biocompatibility, the spontaneous degradation of Mg within the physiological surroundings of the human body makes it a potential candidate for the implant as it denies the second surgery for implant removal post-patient recovery and hence renders the patient significant pain relief and secondary surgery cost (Ref 1-5).

Magnesium, an important element being involved in various biological and metabolic reactions within the body, however, has a relatively fast degradation rate concerning the patient's recovery period alongside excess hydrogen evolution and incremented pH value around the healing sight (Ref 6-8). Apart from the rapid degradation rate, tribo-corrosion would arise due to the tribological implant movement; as a result, the mechanical strength of the implant has to be compromised (Ref 9, 10) even before the patient has healed completely, restricting the clinical applications of pure magnesium. Consequently, the mechanical characteristics and the surface corrosion of magnesium need to be tuned according to the desired application.

Apart from various techniques employed to improve the metal surface performance for implant application, ion implantation is a very simple surface engineering method of potentially functional layers of bioresorbable metals (Ref 2). To comprehend the nature of the interaction of an ion with a solid, the mechanism of the energy loss of the ion in solids has to be understood. When an ion makes an impact on a solid surface and penetrates it, it immediately has to counter a resistive force that continuously opposes the forward motion of the ion, as a result slowing it down and eventually stopping it. This force is termed as the *stopping power or the energy loss* of the solid.

The various energy loss processes occurring due to different effects result in either scattering or the stoppage of the ion in the solid. The current discussion focuses only on the elastic collision of the ions with the target nuclei termed as the *nuclear stopping power or elastic energy loss* being the dominating energy loss process for low energy ions (∼ keV/amu) (Ref 11-13) which is the case for the current study. With the help of ion beam irradiation, many nanoscale features such as cell adhesion can be easily induced on the surface of a bioresorbable metal such as Mg. The simultaneous implantation of ions and sputtering of the substrate surface atoms leads to self-organized features on the surface. The geometry and dimensions of those

features are controllable by varying certain factors associated with the ion beam incident on the target surface such as mass, energy, temperature, the angle of incidence, and the fluence (Ref 14-17).

As it has been demonstrated experimentally, ion implantation of certain elements such as carbon, nitrogen, and oxygen has depicted the improved surface degradation resistance and biocompatibility of various metals such as aluminum, titanium and stainless steel *in vivo* as well as *in vitro* (Ref 18-26). An abrasive surface is developed as a result of ion implantation, and a perfect binding force adheres to the improved surface and the remaining material matrix without modifying the substrate dimensions (Ref 25, 27). In the recent past, it has been demonstrated that implantation of several metallic ions such as Al (Ref 28, 29), Ti (Ref 30) and Zr (Ref 31), etc., and non-metallic gaseous elements such as O_2 (Ref 32), H_2 (Ref 33) and N_2 (Ref 34), etc., into magnesium and its alloys have decelerated their corrosion. For enhancing the corrosion resistance without reducing the biocompatibility and mechanical properties of magnesium for medical applications, the element to be implanted into the magnesium substrate is very important (Ref 35).

Phosphorous an essential nutrient element in calcium phosphate which is a major constituent of the human bone growth material has been implanted in conventional biocompatible materials such as titanium (Ref 36, 37), and the structure of the phosphate layer formed over the pure magnesium surface after the ion implantation was analyzed (Ref 38-42). The phosphorous atoms seem to sit in the interstitial sites of the substrate (Ref 38), and forming a titanium phosphide (TiP) layer has been studied (Ref 39). For the TiP layer on top of titanium, the P ions were implanted above a certain threshold fluence value below which the P ions refused to penetrate the titanium surface. The TiP thickness increased with increased P fluence. The ion beam energy and fluence values determine the thickness of the implanted layer without any titanium-phosphorous compound making the surface partially amorphous (Ref 40, 43). Moreover, surface phosphorylation has demonstrated the improvement in the corrosion resistance and biocompatibility of magnesium-based materials to form the phosphate layer over the magnesium surface. A coating of phytic acid (PA) on the WE43 alloy of magnesium has improved the cytocompatibility and reduced the hemolysis ratio of the coated alloy to meet the standards of the bioresorbable metals (Ref 20). The work presented in the current study was aimed at optimizing the surface morphological and electrochemical properties of pure magnesium like biocompatibility, mechanical strength and corrosion resistance in an in vitro environment such as simulated body fluid to simulate the strong physiologically reactive conditions when Mg-based implants are implanted inside the patient's body.

2. Experimental

2.1 Sample Preparation and Ion Implantation

This study focused on pure magnesium which was implanted with pure phosphorous ions. Before implanting the ions, the as-cast pure magnesium was electrically wire cut into blocks with dimensions 12.5 × 12.5 × 1.7 mm, and the blocks were ground with increasing grit values from 700 to 1500 SiC paper and then polished with diamond paste. The polished samples were cleaned ultrasonically in acetone and with ethanol and finally dried in air. The phosphorous ions were implanted into magnesium samples using a Pelletron linear accelerator (Model: 5UDH-2 NEC, USA) installed at The National Centre for Physics (NCP), Islamabad, Pakistan, at room temperature with a target chamber vacuum of $\sim 10^{-5}$ Pa on one side of the sample with an accelerating ion beam energy of 700 keV and ion-beam current density of 2 μA/cm^2. The typical fluence values for the implantation were 10^{15}, 10^{16} and 10^{17} ion/cm^2 as the range of fluence for effective ion implantation in metals is 10^{16}-10^{18} ions/cm^2. Fluences above this range can lead to crystallographic dislocations and point defects, whereas below the range values can make no significant impact on the substrate surface (Ref 2, 3).

Table 1 Simulated body fluid (SBF) chemical composition

Reagent	Amount
$NaHCO_3$	0.35 (g/L)
NaCl	8.0 (g/L)
$CaCl_2$	0.27 (g/L)
$K_2HPO_4.3H_2O$	0.21 (g/L)
$MgCl_2.6H_2O$	0.33 (g/L)
KCl	0.45 (g/L)
Na_2SO_4	0.068 (g/L)
Glucose	1.1 (g/L)
$MgSO_4.7H_2O$	0.24 (g/L)

2.2 Optimization/ Characterization Techniques

The surface morphological analysis to understand the surface structure of the sample pre- and post-ion implantation was done by the atomic force microscope (AFM) using a Nano Surf 3000 Flex-AFM instrument with tip size of 20 nm, scan size $\sim$ 1 μm and scan rate of 1 Hz. The Gwyddion software used for AFM image processing was employed to extract the 3D images. The crystal structure of the pure sample and post-implantation was revealed by grazing incidence x-ray diffraction (GIXRD) analysis with the help of a x-ray diffractometer (Model: D8 Advance, Bruker, Germany) having Cu-Kα radiation source (λ=0.15 nm) which was used for phase analysis with the grazing angle between the sample and the source set at 2°. The energy of the x-ray beam was of 40 keV and current of 20 mA. The XRD patterns were recorded in the scanning range of 2θ=20°-80° at a scan rate of 0.001°/min and step size of 0.02°. The XRD profiles of the samples have been taken at the room temperature. The results were interpreted through JCPDS reference cards in X'pert high score software, respectively. The percentage concentrations for the implanted ions according to the depth from the sample surface were revealed by the energy-dispersive x-ray diffraction spectroscopy (EDS). Surface hardness and elasticity measurements were conducted by a nano-indenter adjusting it in the continuous stiffness measurement (CSM) mode with the indentation depth set at 1200 nm at the velocity of approach nearing the sample surface around 40 nm s^{-1} with the frequency of 35 Hz. The surface tribological characteristics of the sample were examined by a friction-abrasion testing machine and a standard steel ball (diameter, 12.3 nm) pre-

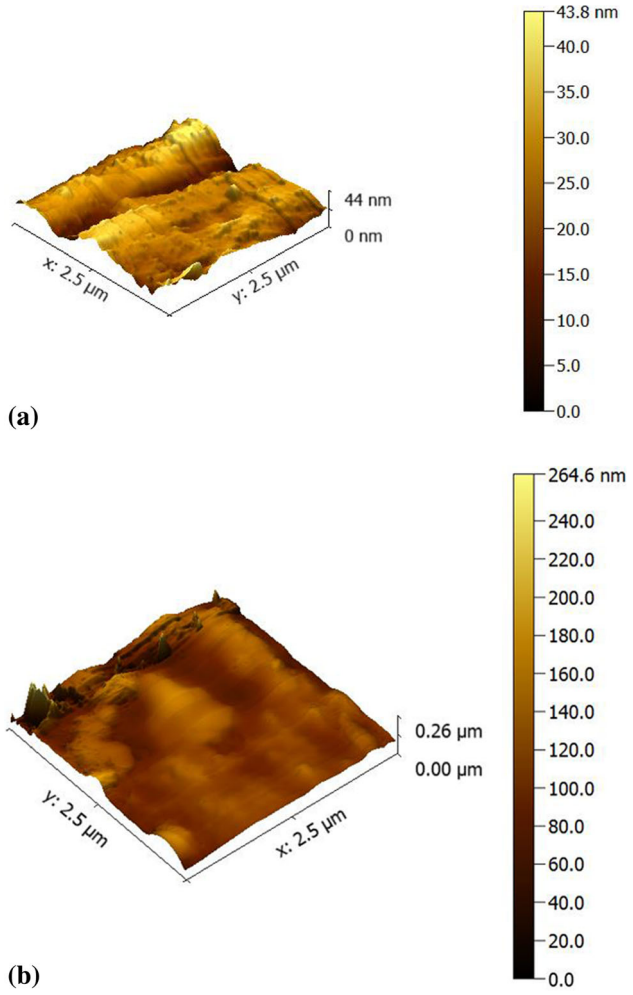

Fig. 1 AFM images of (a) pure Mg; (b) P-implanted Mg

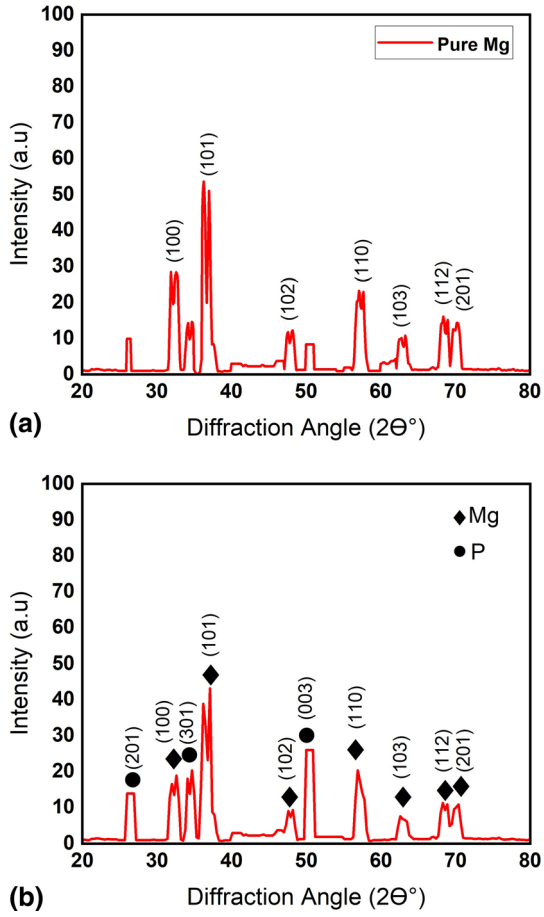

Fig. 2 XRD plots of (a) pure Mg; (b) P-implanted Mg

and post-implantation in the simulated body fluid. The analysis had been executed with a constant normal load of 4 N as the standard normal load values range from 3 to 5 N (Ref 2, 3) and the sliding speed of 10 mm s^{-1} along with a duration of 5 minutes, respectively. The scanning electron microscope revealed the surface structure post-ion implantation.

The simulated body fluid (SBF) was used to conduct the *in vitro* degradation tests of both the pure and the implanted sample surface where the SBF was maintained at the normal human body temperature of 37 °C and a pH of 7.3 which is close to the normal physiological value. The chemical composition of the SBF is given in Table 1.

Three-electrode cells work station comprises of the saturated calomel electrode (SCE) as the reference electrode, a platinum mesh being the counter electrode, while the sample being the working electrode was used for the electrochemical analysis of the implanted samples. The surface area exposed to the electrolyte was about 1.56 cm^2, and the sides of the sample were covered with epoxide resin so that only the implanted surface will be exposed to the SBF. The polarization curves have been obtained at a scanning potential rate of 4 mV s^{-1} from −2.0 to −1.0 V. The corrosion potential (E_{corr}) and the corrosion current density (I_{corr}) had been determined by the Tafel extrapolation of the cathodic polarization curve as the cathodic curve had depicted a better Tafel region as compared to the anodic curve.

Table 2 Experimental vs. standard database for Mg and P (a comparison)

		Diffraction angle 2θ°		
Element	**Peak number**	**Current study**	**Database**	**hkl**
Magnesium	1	32.6	32.1	100
	2	37.1	36.6	101
	3	48.2	47.8	102
	4	56.9	57.3	110
	5	62.6	63.0	103
	6	68.6	68.3	112
	7	70.4	70.0	201
Phosphorous	1	26.6	26.3	201
	2	34.7	34.4	301
	3	51.6	52.1	003

3. Results and Discussion

3.1 Morphological Analysis

Figure 1(a) and (b) shows the 3D images of Atomic Force Microscopy (AFM) of un-implanted and P-implanted magne-

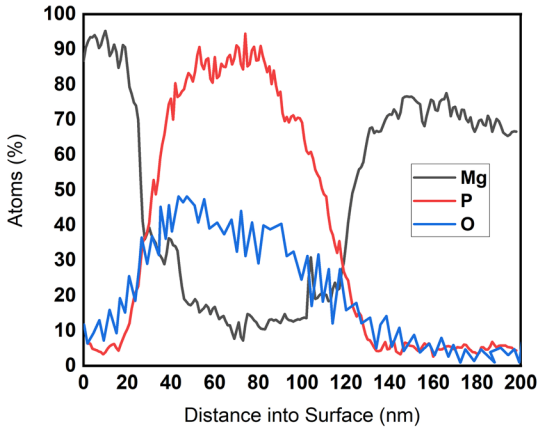

Fig. 3 EDS plots of Mg implanted with P

sium surfaces, respectively, with varying morphological structures. As it can be seen, there are obvious inhomogeneous scratches that emerged as a result of mechanical polishing (Fig. 1a). The phosphorous implanted Mg surface shown in Fig. 1b depicts more homogeneous scratches distributed over the surface of magnesium. The root mean square (RMS) values of surface roughness have significantly been decreased from 44 nm to 26 nm post-ion implantation mainly due to morphological restructuring as the surface temperature elevates during ion implantation (Ref 5).

The observed XRD patterns for both the pure and P-implanted magnesium are shown in Fig. 2(a) and (b), respectively. The samples were crystallite without any amorphous phases observed as confirmed by comparison between the XRD data obtained in this work and the database (Ref 44, 45) for both magnesium and phosphorous as shown in Table 2. For Mg, a total of seven peaks were observed. The highest peak intensity was observed against the diffraction angle of 70.4°, followed by the second and third highest peaks at 68.6° and 62.6°, respectively. Similarly phosphorous phase showed the highest peak intensity for 51.6°. The x-ray diffraction (XRD) patterns of pure and P-implanted Mg samples are shown in Fig. 2. The comparison between characteristic XRD peaks of pure and P-implanted Mg at their corresponding angles of diffraction shows the presence of the desired implanted ions into the Mg substrate. Moreover, the peak intensities rise with the incremented fluence values indicating the increase in the concentration of implanted ions as expected post-implantation.

The energy-dispersive X-ray spectrum EDS plots shown in Fig. 3 revealed that the implanted P ions settled around within a depth from 20 nm to 130 nm under the surface. For the in-depth comprehension of slow ion–target material interaction, the encounter can be sequentially subdivided into three stages occurring at various time scales (Ref 46-48): the incident ion or projectile energy deposition to the electrons of the magnesium metal, energy distribution from the electronic organization to the atomic lattice structure of the target material and finally the atomic movement.

At the initial stage, the potential energy carried by the incident projectiles will be imparted directly to the electrons of the target material where some of the target electrons are ejected out of the target material carrying the imparted energy as their kinetic energy. A charged ion nearing the target surface has to undergo numerous processes of neutralization and de-excitation. The electrons from the target are taken up by the

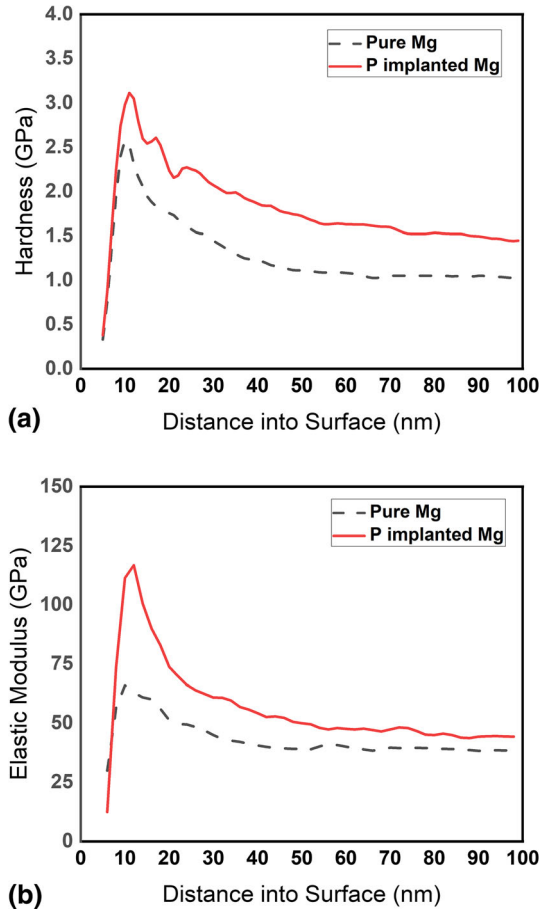

Fig. 4 (a) Hardness and (b) elastic modulus vs. displacement into the sample surface curves of pure and P-implanted Mg

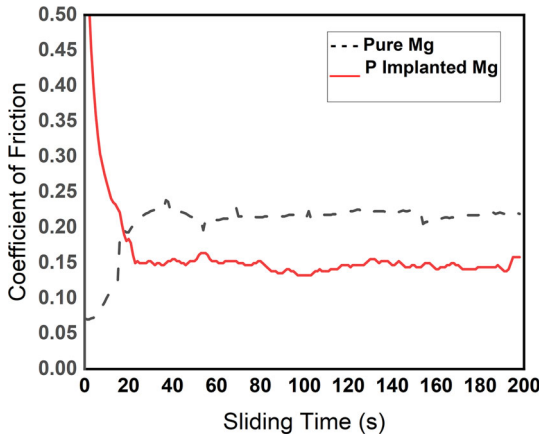

Fig. 5 The coefficient of friction vs. sliding time of pure and P-implanted Mg in SBF

projectile to its excited states from where they can adopt various modes of decay such as the Auger process, collisions, or emission of radiation. This interaction results in the weakening of the target structure as some unbalanced holes are produced in the target surface capable of storing a fraction of the imparted energy during a collision. A projectile landing at the target surface spends a very short time at the surface as

the projectile being in an extremely excited state and penetrates further into the target before absolute relaxation. This is the stage when electrons will jump into some intermediate excited states either by resonant charge transfer from the valence band or Auger neutralization immediately following the Auger de-excitation sequence. As a result of this sequence, low-energy electrons ranging up to a few hundred electron volts are ejected. For the inner shell holes to be filled, electrons with energies of keV kinetic energy should make transitions (Ref 49, 50).

In the second step, a Monte Carlo type electron transport simulation is applied in which elastic as well as inelastic scattering is considered with trajectories of secondary electrons being followed. Ultimately as a result of phonon excitation during collisions between electrons and the lattice atoms a surge in the lattice temperature will be induced. Melting needs a relatively high energy density which is available in the proximity of the ion trajectory where dominantly low energy electrons have a significant role. For the high-energy electrons having relatively longer mean free path for both their elastic and inelastic collisions, the distribution of energy spans over longer volumes (Ref 51, 52).

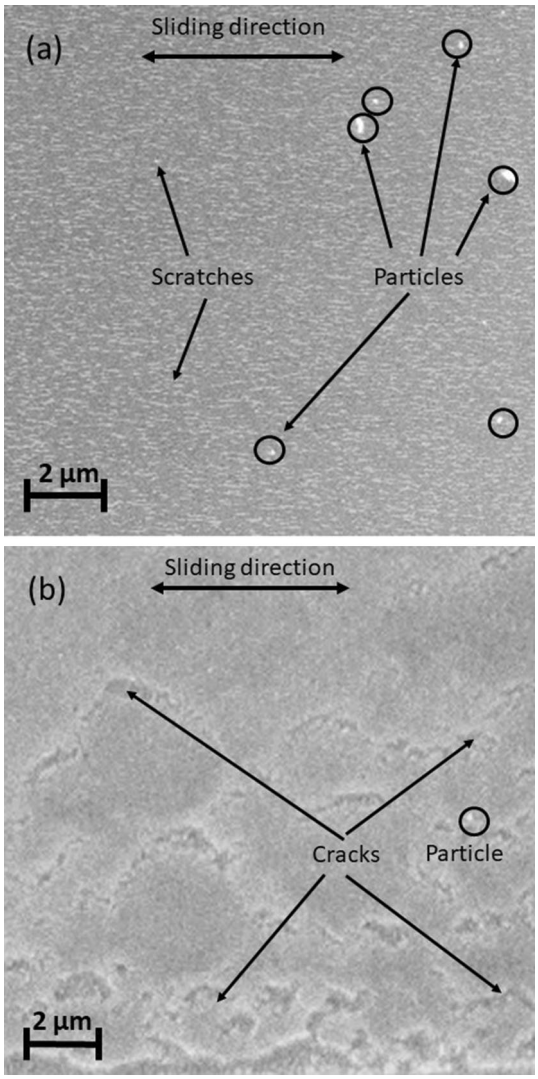

Fig. 6 SEM images of wear surfaces for (a) pure and (b) P-implanted Mg

The final step describes the lattice restructuring which takes place on a picosecond time scale. With the aid of molecular dynamic (MD) simulations, the melting and cooling phases can be understood in detail. These simulations when employed (Ref 53) gave appreciable results which agreed with the demonstrated threshold values alining the potential energy threshold measured for CaF_2 for nanoscale melting at the surface. These simulations also proved that the process is entirely dependent on the potential energy being deposited initially to the top few target layers and is independent of the kinetic energy of the incident ion beam. As a conclusion, the size of the observed surface structures primarily remains invariant with the kinetic energy of the striking ions.

Moreover, the presence of oxygen was also confirmed from top to a certain depth from the substrate surface especially close to the depth of P. The passive MgO and $Mg(OH)_2$ films on top of the substrate surface are the reason for O atoms present above the implanted P atoms layer. This passive film is only a few nanometers in thickness (Ref 3), and hence, the desired ions are implanted through this passive layer. Also, the O atoms present as an impurity in the source material may have been carried into the substrate material in the process of implantation.

3.2 Mechanical Analysis of P-Implanted Mg

The graphs of surface hardness and the elastic modulus against the distance into the magnesium surface before and implanting phosphorous ions are shown in Fig. 4(a) and (b) respectively. It is obvious from the graphs that the surface hardness and elastic modulus initially are incremented with depth into the sample surface to attain peak values and then gradually decrease settling to near-constant values for both pure and implanted samples. In comparison with the pure sample, the P-implanted sample surface depicted increased values of the surface hardness and the elastic modulus mainly due to work hardening layer formation as a result of ion bombardment of P ions in the process of implantation (Ref 3). Moreover, the maximum values of 3.12 and 117.17 GPa at a depth of around 11 nm have been recorded for the surface hardness and the elastic modulus, respectively, of the post-implantation in the sample which agrees with the EDX graphs shown in Fig. 3. The experimental results depicted that the surface hardness and elastic modulus could essentially be enhanced through P ion implantation in pure Mg.

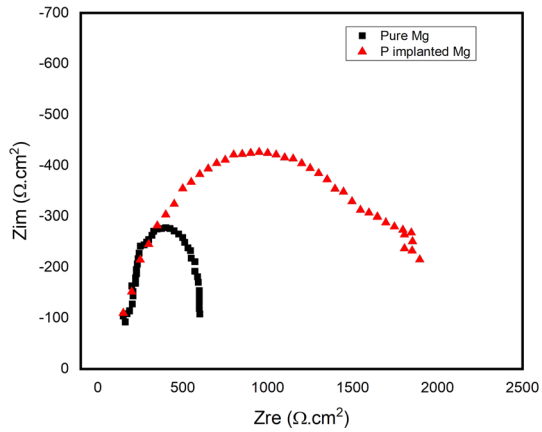

Fig. 7 Nyquist plots for pure and P-implanted Mg in SBF

Figure 5 shows the coefficient of friction vs sliding time graph comparing the pure with the P-implanted samples. It was observed that initially, the coefficients of friction curves have a varying range, and then it tends to get nearly unvarying values for the rest of the sliding times. The P-implanted Mg surface has lower friction coefficient values in comparison with the pure surface mainly due to more powerful bearing capacity due to improved surface hardness attributed to post-P ion implantation measured by nano-indentation.

After performing the friction wear tests in SBF, SEM micrographs of wear morphologies of both pure and P-implanted sample surfaces are shown in Fig. 6(a) and (b), respectively. Some scratches, cracks, parallel grooves, and tiny particles were seen on the sample surface. Tiny particles might have been the oxide particles formed during sliding which is typically due to the corrosion wear. These abrasive grains are there to contribute to the development of grooves during abrasive wear. As a result, the surface wear process of friction consists of both abrasive and corrosion wear, and the wear scar of the surface has been significantly enhanced by P ion implantation as indicated in Fig. 6(b).

3.3 Electrochemical Analysis of P-Implanted Mg

Figure 7 demonstrates the Nyquist plots for the electrochemical impedance spectroscopy (EIS) analysis for both the pure and P-implanted Mg samples. The Nyquist plots of the pure Mg exhibited three loops with three time constants: first, a high area semicircle for high frequency, second, a low sized loop for the intermediate frequency and finally an inductance loop for low frequency. The charge transfer resistance attributed to the SBF-sample surface interface had resulted as the high frequency capacitive loop. The mass transport linked to the ion diffusion across the corrosion product layer is depicted by the intermediate frequency capacitive loop. Finally, the low frequency inductive loop is related to the adsorption process of the corrosion products in the surface pits (Ref 54, 55). Also a couple of capacitive loops were observed, one in the high frequency region and the other in the low frequency region for the P-implanted Mg. The loops were attributed to the charge transfer resistance and the mass transport due to ion diffusion through the corrosion product layer, respectively. Due to the fact that the diameter of the loop is related to the corrosion resistance and a high sized loop represents improved corrosion resistance (Ref 55) shown in Fig. 7, P-implanted Mg depicted high capacitive loops with improved corrosion resistance in SBF.

The equivalent circuits for describing the electrochemical reactions occurring on the interface of the electrode and the solution for both the pure and the treated Mg surfaces are

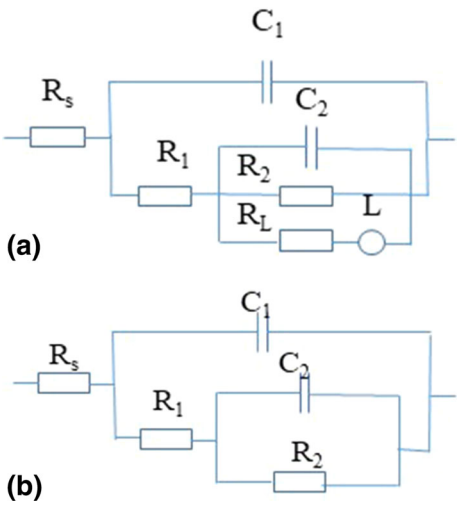

Fig. 8 Equivalent electrical circuits for (a) pure and (b) P-implanted Mg for EIS analysis in SBF

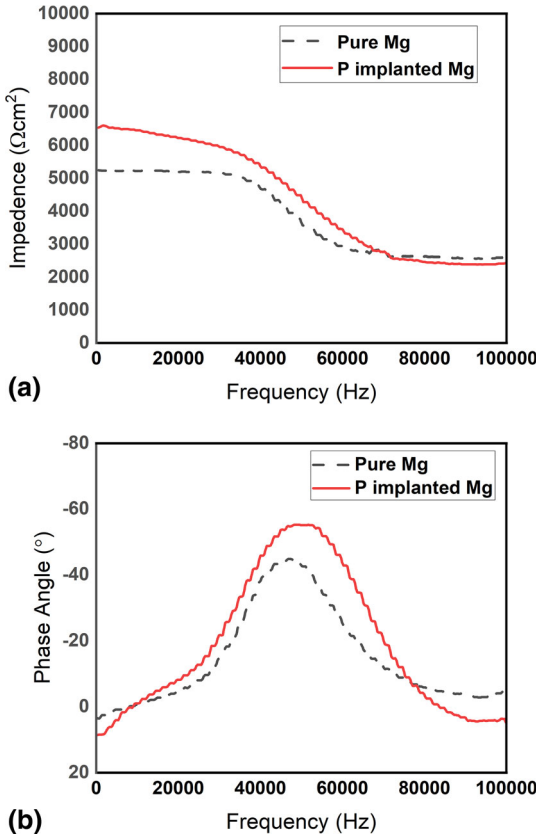

Fig. 9 (a) Bode impedance and (b) phase angle vs. frequency of pure and P-implanted Mg in SBF

Table 3 The corresponding equivalent circuit element values for the pure and P-implanted Mg in SBF for the EIS analysis

Sample	R_s, Ωcm^{-2}	C_1, $\Omega/cm^2.S^n$	n_1	R_1, Ωcm^{-2}	C_2, $\Omega/cm^2.S^n$	n_2	R_2, Ωcm^{-2}	L, hcm^{-2}	R_L, Ωcm^{-2}
Pure Mg	66.47	1.072×10^{-5}	0.82	49.39	1.041×10^{-5}	0.79	359.38	3247	245.5
P implanted Mg	69.38	1.713×10^{-5}	0.54	1687	5.273×10^{-4}	1	389.89		

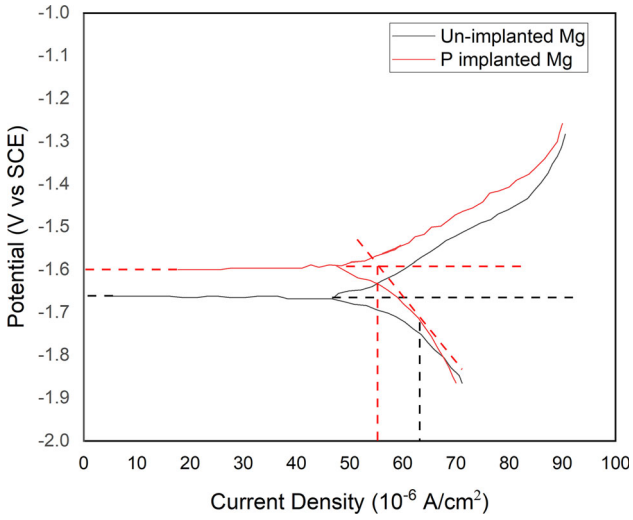

Fig. 10 Corrosion potential vs. current density curves of pure and P-implanted Mg in SBF

Table 4 Corrosion potentials (E_{corr}) and corrosion current densities (I_{corr}) of pure Mg and P-implanted Mg in SBF from polarization curves

Sample	E_{corr}, V Vs SCE	I_{corr}, 10^{-6}cm^{-2}
Pure Mg	−1.657	67.601
P-implanted Mg	−1.598	54.955

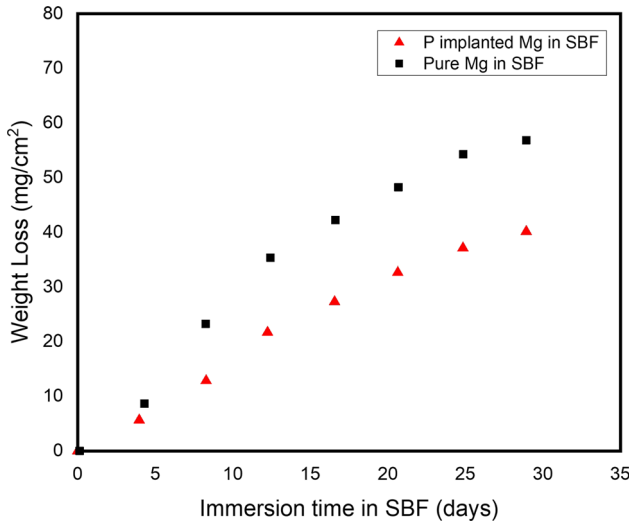

Fig. 11 Weight loss vs immersion time plot of pure and P-implanted Mg in SBF

shown in Fig. 8(a) and (b), respectively. For this equivalent circuit, the solution resistance between the reference electrode and the working electrode is given by R_s, the double layer capacitance between the corrosion product layer or the surface oxidized layer and the solution has been represented by a constant phase element, C_1, R_1 shows the corresponding electrolyte resistance, R_2 gives the charge transfer resistance. In

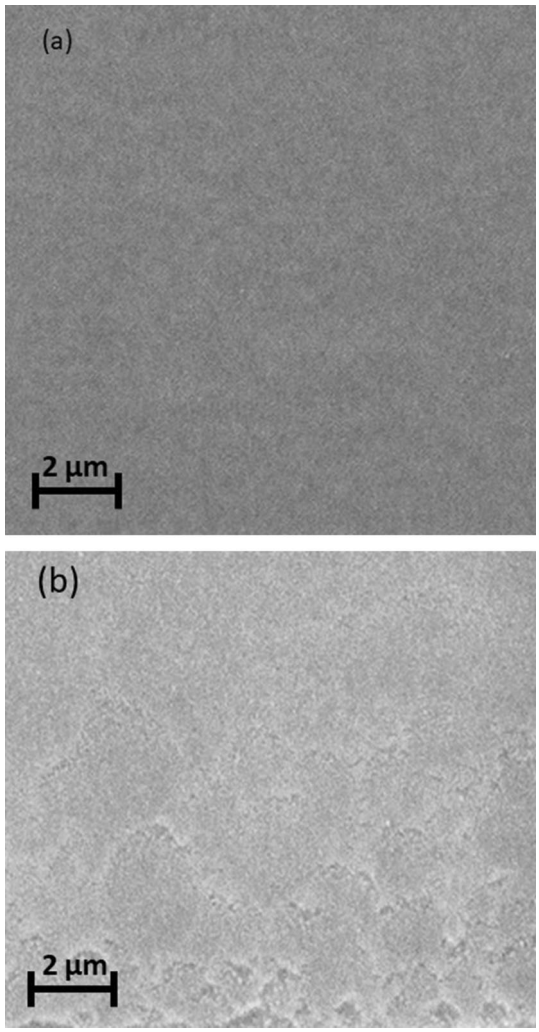

Fig. 12 SEM for surface morphology of (a) pure and (b) P-implanted Mg in SBF

the similar equivalent circuit diagrams reported earlier (Ref 41, 54, 55), the inductive resistance and the inductance possibly due to pitting corrosion or to the adsorption effect have been shown by R_L and L, respectively (Ref 2). Table 3 indicates the corresponding fitted EIS values. The diffusion process of electrolytes by the oxidized surface layer or the corrosion product layer has been displayed by R_1, whereas R_2 depicts the dissolution rate of the pure Mg. R_1 and R_2 values for the pure Mg were quite low in comparison with the *P*-implanted Mg. The reason behind these low values could be the initial dissolution of the pure Mg porous $Mg(OH)_2$ layer formation during the commencing immersion process allowing the corrosive medium to channel through at the substrate surface and cause underneath corrosion. Also the higher values of R_1 and R_2 for the P-implanted Mg are mainly due to the dense magnesium oxide and phosphorous oxide layers formed post-P ion implantation on the Mg substrate. These layers provide an effective protective layer against corrosion. The accumulative resistance (sum of R_1 and R_2) is a quantitative measure of the corrosion resistance of a material (Ref 55, 56). As compared, the accumulative resistance of P-implanted Mg (2076.89 $\Omega.cm^{-2}$) corresponding to the pure Mg (408.77 $\Omega.cm^{-2}$) was found to be about 5 times higher. This clearly suggests a slower

corrosion rate in SBF due to the surface modified layers comprising of phosphorous and magnesium oxides post-P ion implantation.

A comparison of Bode impedance vs frequency and phase angle vs frequency of pure and P-implanted Mg in SBF is depicted in Fig. 9(a) and (b) respectively. According to Fig. 9(a), the impedance of P-implanted Mg exceeds pure Mg for almost the whole range of frequencies between 500 Hz and around 7 kHz indicating the fact that P-implanted Mg has an improved corrosion resistance mainly because of the passive phosphorous oxide layer formation post-implantation resulting in the blockage of the charge transfer process during corrosion which results in improved corrosion resistance. Figure 9(b) shows a higher degree of phase angle for P-implanted Mg in comparison with pure Mg for a range of frequencies between about 8 and 80 kHz attributed to the protective layer present over the substrate surface after P ion implantation. The peak phase angles of pure and P-implanted Mg were observed to be $-44°$ and $-55°$, respectively, where the higher phase angle describes a better corrosion resistance after implantation.

The corrosion potential vs current density curves of pure and P-implanted Mg in SBF are shown in Fig. 10 with the values of the corresponding corrosion potential (E_{corr}) and the corrosion current density (I_{corr}) tabulated in Table 4. A lower corrosion tendency has been indicated with P-implanted Mg in comparison with the pure Mg due to E_{corr} shifting towards the noble direction. Moreover, when the potential limit is crossed, more pitting corrosion dominates in the corrosion behavior. Also, the phosphorous implanted magnesium had a lower current density I_{corr} of (55 μAcm^{-2}) in comparison with pure Mg indicating the fact that a lower current density is a major indicator of corrosion resistance. Consequently, the corrosion resistance of pure magnesium has improved after phosphorous ion implantation.

The weight loss calculations for both the pure and the P-implanted Mg samples in SBF have been estimated using the following relation (Ref 57):

$$\text{Weight Loss}(W) = \frac{w_o - w_p}{A}$$

where W is the weight loss in mg/cm^2, w_o and w_p are the weights of the pure and the P-implanted Mg samples after immersion in SBF, respectively, and A is the exposed sample surface area in cm^2.

The galvanometric technique was employed to investigate the progressive weight loss of the pure and the P-implanted Mg samples after immersion in SBF for 30 days, and Fig. 11 reveals the weight loss vs time plots of both the samples. The weight loss of pure Mg is significantly higher ($\sim$55 mg/cm^2) than the treated sample ($\sim$40 mg/cm^2) attributed to formation of the passive MgP and MgO (Ref 55, 56) protective layers which being less reactive than pure Mg in more corrosive SBF environment.

Surface morphology of pure and phosphorous implanted magnesium post-immersion in SBF for 30 days is depicted in Fig. 12(a) and (b), respectively. Because of chloride ions in SBF, a damaged surface sustaining certain cracks and pits is observable from the pure and phosphorous implanted magnesium which is typically due to the local corrosion. In comparison with the pure magnesium, some lower-sized cracks and a few pits on phosphorous implanted magnesium surface have shown minor damage after immersion. The observed surface has served as an evidence for the enhancement of corrosion resistance of P-implanted Mg in SBF. The enhanced corrosion resistance can be regarded as the fact that the presence of the dense oxide layers comprise of PO and MgO, providing a good protection layer for pure magnesium in SBF.

4. Conclusions

Pure magnesium was bombarded by phosphorous ions using a Pelletron accelerator resulting in an approximately 120-nm-thick layer primarily composing of PO along with MgO had formed on the surface of pure Mg. The surface morphology demonstrated relative smoothness post-implantation. The Mg surface was altered to higher values of hardness, elastic modulus and enhanced wear resistance corresponding to a wear mechanism of abrasive wear following P ions implantation as compared to the naive Mg surface. After immersion in SBF, the E_{corr} value tilted towards the nobler direction, while an appreciable decrement in the corrosion current density I_{corr} depicted that P-implanted Mg has increased corrosion resistance as confirmed by the SEM images. In a nutshell, it is concluded that P ion implantation is a reasonable option for optimizing the mechanical properties and corrosion resistance of pure Mg for biomedical implant applications.

Acknowledgments

The authors acknowledge the technical assistance of the School of Biomedical Engineering and Health Sciences, Universiti Teknologi Malaysia, National Center for Physics Islamabad, and GIK Institute of technology Topi, Pakistan.

References

1. H.J.P.I.B. Hermawan, Updates on the Research and Development of Absorbable Metals for Biomedical Applications, *Prog. Biomater.*, 2018, **7**(2), p 93–110
2. Y. Jia et al., Surface Properties of Magnesium Improved by Sr Ion Implantation, *Mater. Res. Exp.*, 2018, **5**(6), p 066546
3. S. Somasundaram, M. Ionescu, and B.K.J.M. Mathan, Ion Implantation of Calcium and Zinc in Magnesium for Biodegradable Implant Applications, *Multidiscip. Digit. Publ. Inst. (MDPI)*, 2018, **8**(1), p 30
4. J. Yang et al., A Review on the Exploitation of Biodegradable Magnesium-Based Composites for Medical Applications, *Biomed. Mater.*, 2018, **13**(2), p 022001
5. R. Xu et al., Eelectrochemical Properties and Corrosion Resistance of Carbon-Ion-Implanted Magnesium, *Corros. Sci.*, 2014, **82**, p 173–179
6. N. Kirkland, N. Birbilis, and M.J.A.B. Staiger, Assessing the Corrosion of Biodegradable Magnesium Implants: A Critical Review of Current Methodologies and Their Limitations, *Acta Biomater.*, 2012, **8**(3), p 925–936
7. Z. Xiaobo et al., Microstructure, Mechanical and Corrosion Properties of Mg-(4–x) Nd-xGd-Sr-Zn-Zr Biomagnesium Alloys, *Sci. Press*, 2014, **50**(8), p 979–988
8. Z.U. Rahman, L. Pompa, and W.J.J.O.M.S.M.I.M. Haider, Electrochemical Characterization and In-Vitro Bio-Assessment of AZ31B and AZ91E Alloys as Biodegradable Implant Materials, *J. Mater. Sci. Mater. Med.*, 2015, **26**(8), p 1–11
9. Wilson, J.J.F.B.M., Metallic Biomaterials: State of the Art and New Challenges. Fundam. Biomater. Metals, 2018: 1-33
10. N. Manam et al., Study of Corrosion in Biocompatible Metals for Implants: A Review, *J. Alloy. Compd.*, 2017, **701**, p 698–715
11. M.A. Shafique et al., Effect of Doping Concentration on Absorbance, Structural, and Magnetic Properties of Cobalt-Doped ZnO Nano-Crystallites, *Int. Nano Lett.*, 2012, **2**(1), p 1–7

12. M. Nastasi et al., *Ion-Solid Interactions: Fundamentals and Applications*, Cambridge University Press, Cambridge, 1996
13. H. Ryssel and I. Ruge, *Ion Implantation*, John Wiley & Sons, Chichester, 1986
14. J. Muñoz-García et al., Self-organized surface nanopatterning by ion beam sputtering, *Toward Functional Nanomaterials*. Springer, Berlin, 2009, p 323–398
15. M. Castro et al., Self-Organized Ordering of Nanostructures Produced by Ion-Beam Sputtering, *Phys. Rev. Lett.*, 2005, **94**(1), p 016102
16. S.U. Awan et al., Correlation Between Structural, Electrical, Dielectric and Magnetic Properties of Semiconducting Co Doped and (Co, Li) Co-Doped ZnO Nanoparticles for Spintronics Applications, *Physica E*, 2018, **103**, p 110–121
17. S.U. Awan et al., Room Temperature p-Type Conductivity and Coexistence of Ferroelectric Order in Ferromagnetic Li Doped ZnO Nanoparticles, *J. Appl. Phys.*, 2014, **116**(16), p 164109
18. N. Ali et al., Assessment of Fatigue and Corrosion Fatigue Behaviours of the Nitrogen Ion Implanted CpTi, *Int. J. Fatigue*, 2014, **61**, p 184–190
19. K. Feng et al., Improved Corrosion Resistance of Stainless Steel 316L by Ti Ion Implantation, *Mater. Lett.*, 2012, **68**, p 450–452
20. P. Tian and X.J.R.B. Liu, Surface Modification of Biodegradable Magnesium and its Alloys for Biomedical Applications, *Regen. Biomater.*, 2015, **2**(2), p 135–151
21. H. Wang et al., Improvement of In Vitro Corrosion and Cytocompatibility of Biodegradable Fe Surface Modified by Zn Ion Implantation, *Appl. Surf. Sci.*, 2017, **403**, p 168–176
22. M. Esmaily et al., Fundamentals and Advances in Magnesium Alloy Corrosion, *Prog. Mater Sci.*, 2017, **89**, p 92–193
23. A. Adhilakshmi, K. Ravichandran, and S.N.J.N.J.O.C. Tsn, Protecting electrochemical degradation of pure iron using zinc phosphate coating for biodegradable implant applications, *New J. Chem.*, 2018, **42**(22), p 18458–18468
24. X. Wei et al., Improvement on Corrosion Resistance and Biocompability of ZK60 Magnesium Alloy by Carboxyl Ion Implantation, *Corros. Sci.*, 2020, **173**, p 108729
25. S. Bagherifard et al., Effects of Nanofeatures Induced by Severe Shot Peening (SSP) on Mechanical, Corrosion and Cytocompatibility Properties of Magnesium Alloy AZ31, *Acta Biomater.*, 2018, **66**, p 93–108
26. X.W. Tao et al., Nanomechanical and Corrosion Properties of zk60 Magnesium Alloy Improved by gd Ion Implantation, *Surf. Rev. Lett.*, 2014, **21**(06), p 1450085
27. Z. Wang et al., Corrosion Behaviour of Nd Ion Implanted Mg–Gd–Zn–Zr Alloy in Simulated Body Fluid, *Adv. Perform. Mater.*, 2015, **30**(6), p 321–326
28. G. Wu et al., Retardation of Surface Corrosion of Biodegradable Magnesium-Based Materials by Aluminum Ion Implantation, *Appl. Surf. Sci.*, 2012, **258**(19), p 7651–7657
29. M. Lei et al., Wear and Corrosion Resistance of Al Ion Implanted AZ31 Magnesium Alloy, *Surf. Coat. Technol.*, 2007, **201**(9–11), p 5182–5185
30. C. Liu et al., Corrosion Resistance of Titanium Ion Implanted AZ91 Magnesium Alloy, *J. Vac. Sci. Technol. A*, 2007, **25**(2), p 334–339
31. C. Liu et al., Corrosion Behavior of AZ91 Magnesium Alloy Treated by Plasma Immersion Ion Implantation and Deposition in Artificial Physiological Fluids, *Thin Solid Films*, 2007, **516**(2–4), p 422–427
32. G. Wan et al., Corrosion Properties of Oxygen Plasma Immersion Ion Implantation Treated Magnesium, *Surf. Coat. Technol.*, 2007, **201**(19–20), p 8267–8272
33. A. Bakkar and V.J.C.S. Neubert, Improving Corrosion Resistance of Magnesium-Based Alloys by Surface Modification with Hydrogen by Electrochemical Ion Reduction (EIR) and by Plasma Immersion Ion Implantation (PIII), *Corros. Sci.*, 2005, **47**(5), p 1211–1225
34. X.B. Tian et al., Corrosion Resistance Improvement of Magnesium Alloy Using Nitrogen Plasma Ion Implantation, *Surf. Coat. Technol.*, 2005, **198**(1–3), p 454–458
35. R. Asri et al., Corrosion and Surface Modification on Biocompatible Metals: A Review, *Mater. Sci. Eng., C*, 2017, **77**, p 1261–1274
36. D. Krupa et al., Effect of Phosphorus-Ion Implantation on the Corrosion Resistance and Biocompatibility of Titanium, *Biomaterials*, 2002, **23**(16), p 3329–3340
37. D. Krupa et al., Effect of Dual Ion Implantation of Calcium and Phosphorus on the Properties of Titanium, *Biomaterials*, 2005, **26**(16), p 2847–2856
38. S. Ferdjani et al., Phosphorus Implantation in Titanium: Application to Calibration Analysis, *J. Alloy. Compd.*, 1991, **177**(2), p 265–272
39. S. Baunack et al., Depth Distribution and Bonding States of Phosphorus Implanted in Titanium Investigated by AES, XPS and SIMS, *Surf. Interface Anal.*, 1998, **26**(6), p 471–479
40. E. Wieser et al., Modification of Titanium by Ion Implantation of Calcium and/or Phosphorus, *Surf. Coat. Technol.*, 1999, **111**(1), p 103–109
41. H.A. Acciari et al., Surface Modifications by Both Anodic Oxidation and Ion Beam Implantation on Electropolished Titanium Substrates, *Appl. Surf. Sci.*, 2019, **487**, p 1111–1120
42. A. Panepinto, D. Cossement, and R. Snyders, Experimental and Theoretical Study of the Synthesis of N-Doped TiO2 by N Ion Implantation of TiO2 Thin Films, *Appl. Surf. Sci.*, 2021, **541**, p 148493
43. M. Hashmi et al., Effect of Different CaO/MgO Ratios on the Structural and Mechanical Properties of Bioactive Glass-Ceramics, *J. Ceram.-Silikáty*, 2012, **56**(4), p 347–351
44. I. Ismail et al., Determination of the Crystallite Size and Crystal Structure of Magnesum Powder by X-Ray Diffraction, *J. Nat.*, 2020, **20**(3), p 61–65
45. Q. Liu et al., Crystalline Red Phosphorus Nanoribbons: Large-Scale Synthesis and Electrochemical Nitrogen Fixation, *Angew. Chem.*, 2020, **59**(34), p 14383–14387
46. M. Hashmi and S.A.J.P.I.N.S.M.I. Shah, Dissolution Behavior of Bioactive Glass Ceramics with Different CaO/MgO Ratios in SBF-K9 and r-SBF, *Prog. Nat. Sci. Mater. Int.*, 2014, **24**(4), p 354–363
47. F. Aumayr et al., Single Ion Induced Surface Nanostructures: A Comparison Between Slow Highly Charged and Swift Heavy Ions, *J. Phys. Condens. Matter*, 2011, **23**(39), p 393001
48. S. Habenicht, W. Bolse, and K.-P.J.R.O.S.I. Lieb, A Low-Energy Ion Implanter for Surface and Materials Science, *Rev. Sci. Instrum.*, 1998, **69**(5), p 2120–2126
49. Lin, C.-D., *Review of fundamental processes and applications of atoms and ions.* books.google.com, 1993
50. C. Lemell et al., Image Acceleration of Highly Charged Ions by Metal Surfaces, *Phys. Rev. A*, 1996, **53**(2), p 880
51. C. Lemell et al., On the Nano-Hillock Formation Induced by Slow Highly Charged Ions on Insulator Surfaces, *Solid-State Electron.*, 2007, **51**(10), p 1398–1404
52. L. Ali et al., High-Quality Optical Ring Resonator-Based Biosensor for Cancer Detection, *IEEE Sens. J.*, 2019, **20**(4), p 1867–1875
53. A. El-Said et al., Potential Energy Threshold for Nano-Hillock Formation by Impact of Slow Highly Charged Ions on a CaF2 (1 1 1) Surface, *Nucl. Instrum. Methods Phys. Res. Sect. B*, 2007, **258**(1), p 167–171
54. A.J.T. Kand et al., Electrochemical Evaluation of the Hydroxyapatite Coating Synthesized on the AZ91 by Electrophoretic Deposition Route, *Synth. Sinter.*, 2021, **1**(2), p 85–91
55. A.T. Tabrizi et al., Tribological Characterization of Hybrid Chromium Nitride Thin Layer Synthesized on Titanium, *Surf. Coat. Technol.*, 2021, **419**, p 127317
56. A.T. Tabrizi et al., Correction of Archard Equation for Wear Behavior of Modified Pure Titanium, *Tribol. Int.*, 2021, **155**, p 106772
57. M. Rahman et al., Microroughness Induced Biomimetic Coating for Biodegradation Control of Magnesium, *Mater. Sci. Eng. C*, 2021, **121**, p 111811